Rae, J., Andrea, B., Robinson, L., Adkins, J. F., Chen, T., Cole, C., Greenop, R., Li, T., Littley, EFM., Nita, DC., Stewart, J., & Taylor, BJ. (2018). CO_2 storage and release in the deep Southern Ocean on millennial to centennial timescales. *Nature*, *562*(7728), 569-573. https://doi.org/10.1038/s41586-018-0614-0

CO_2 storage and release in the deep Southern Ocean on millennial to centennial timescales

Rae, J.W.B.[1,*], Burke, A.[1], Robinson, L.F.[2], Adkins, J.F.[3], Chen, T.[2,4], Cole, C.[1], Greenop, R.[1], Li, T.[2,4], Littley, E.[1], Nita, D.C.[1,5], Stewart, J.A.[1,2], Taylor, B[1].

1. School of Earth and Environmental Sciences, University of St Andrews, UK.

2. School of Earth Sciences, University of Bristol, UK

3. Division of Geological and Planetary Sciences, California Institute of Technology, USA

4. School of Earth Sciences and Engineering, Nanjing University, China

5. Faculty of Environmental Science and Engineering, Babes-Bolyai University, Cluj-Napoca, Romania

The cause of atmospheric CO_2 change during the recent ice ages remains a first order question in climate science. Most mechanisms have invoked carbon exchange with the deep ocean, due to its large size and relatively rapid exchange time with the atmosphere [1]. The Southern Ocean is thought to play a key role in this exchange, as much of the deep ocean is ventilated to the atmosphere in this region [2]. However reconstructing changes in deep Southern Ocean carbon storage is challenging, so **few direct tests of this hypothesis exist. Here we present new deep-sea coral boron isotope data that track the pH – and thus CO_2 chemistry – of the deep Southern Ocean over the last 40,000 years. At sites closest to the Antarctic continental margin, and most influenced by the deep Southern waters that form the ocean's lower overturning cell, we find a close relationship between ocean pH and atmospheric CO_2: during intervals of low CO_2 ocean pH is low, reflecting enhanced ocean carbon storage; during intervals of rising CO_2 ocean pH rises, reflecting loss of carbon from the ocean to the atmosphere. Correspondingly, at shallower sites we find rapid (millennial to centennial-scale) pH decreases during abrupt CO_2 rise, reflecting the rapid transfer of carbon from the deep to the upper**

ocean and atmosphere. These data thus confirm the importance of the deep Southern Ocean in ice age CO_2 change, and demonstrate that deep ocean CO_2 release can occur as a dynamic feedback to rapid climate change on centennial timescales.

The Southern Ocean may act as a net source of CO_2 from the deep ocean to the atmosphere or a net sink [3], depending on the balance between regional CO_2-supply via circulation and CO_2-removal via biological productivity. Various records have shown that large changes in circulation [4,5] and biological productivity [6] occurred in the Southern Ocean on glacial timescales, with the potential to change the partitioning of carbon between the deep ocean and the atmosphere. However, reconstructions of deep ocean CO_2 storage are currently sparse and more complex. For instance records of CO_2 chemistry from the deep Atlantic [7] and deep Pacific [8] show decreases in carbonate ion saturation and pH during millennial-scale intervals of atmospheric CO_2 rise; in the absence of other processes, low carbonate ion and pH imply an increase in CO_2-storage in the deep ocean, so these signals are thought instead to be dominated by changes in circulation and deep water masses. On longer timescales, records from the deep Indo-Pacific [9] appear to reflect changes in CO_2-storage, but are damped by the buffering influence of carbonate compensation. Records of deep ocean CO_2 chemistry that clearly demonstrate CO_2 storage during atmospheric CO_2 fall, and CO_2 release during atmospheric CO_2 rise, have proved elusive.

Here we test the hypothesis that carbon storage in the deep Southern Ocean played a key role in ice age CO_2 change, with new boron isotope ($\delta^{11}B$) data from uranium-thorium dated deep-sea corals from the Drake Passage (Figure 1; Methods)[4]. The boron isotope pH proxy (see Methods) provides a sensitive measure of the ocean carbonate system, closely tracking CO_2 concentrations and reflecting the ratio of the two master variables, dissolved inorganic carbon (DIC) and alkalinity. Although full reconstruction of the carbonate system

requires knowledge of a second parameter, it is unlikely that alkalinity was lower in the glacial ocean [10], or varied as dynamically as DIC, so our δ^{11}B-pH record may be largely attributed to changes in carbon storage. Note that as our δ^{11}B record extends beyond the pH calibration possible in modern *D. dianthus* (Figure S5) we focus our discussion on relative changes in pH as traced by coral δ^{11}B, and provide absolute pH estimates in Figure S1 for reference. Our sample sites reflect distinct volumes of the deep ocean [11]: the "lower cell" sites lie close to the Antarctic continental margin, bathed by waters that plumb the mid to lower depths of the deep ocean; the "upper cell" sites lie on lighter isopycnal surfaces, bathed by waters found at shallower depths in the ocean basins (Figure 1).

During the LGM and early deglaciation we see a clear gradient between the lower cell sites, which show low δ^{11}B and pH, and upper cell sites, with relatively high δ^{11}B and pH (Figure 2). This supports the idea that during glacial intervals the deep ocean – and its carbon – was more stratified into two cells with limited interaction [11]. Our data show that the lower cell was rich in carbon compared to the upper cell and compared to modern values expected at this site (Figure 1, S1), providing strong support for the hypothesis that the deep glacial ocean sequestered carbon from the upper ocean and the atmosphere [2].

During the deglaciation this gradient in deep carbon breaks down, with lower cell pH rising in step with atmospheric CO_2, and pH in the upper cell falling towards lower cell values (Figure 3). This provides direct evidence for the transfer of carbon from the deep ocean to the upper ocean and the atmosphere. Carbon transfer to the upper ocean appears particularly pronounced at ~14.7 and ~11.7 ka, coincident with the centennial-scale jumps in atmospheric CO_2 [12] associated with abrupt warming in the Northern Hemisphere. This provides the first evidence of a fast teleconnection between abrupt changes in the North Atlantic and the carbon chemistry of the deep Southern Ocean. Lower cell *D. dianthus* samples have not been found

in the Holocene (see Methods), but the available data at the end of the deglaciation and in the modern water column suggest much weaker pH gradients, consistent with less-pronounced property gradients in the modern deep ocean compared to the glacial [11,13,14].

Our data show that the carbonate chemistry of the deep Southern Ocean was closely linked to atmospheric CO_2 change over the last 40 ka. These data thus provide a crucial missing piece of the glacial CO_2 puzzle: the most direct evidence to date of deep Southern Ocean carbon storage and release, as previously inferred from physical properties [5,13], carbon isotopes [15], and oxygen content [16] (Figure 2 & S3). While other processes [3] and regions [8] may contribute to the full magnitude of glacial-interglacial CO_2 change, our data demonstrate a key role for the Southern Ocean on millennial to centennial timescales.

Several processes may contribute to the changes in CO_2 storage observed in our record, including changes in ventilation [4,16], biological pump efficiency [6], and sea ice [17] (Figure S3). We note a close correspondence between lower cell pH and ice core sea salt sodium, a proxy that may reflect changes in sea ice production [18 19] (Figure 2), suggesting that sea ice may play an important role in CO_2 change. Sea ice has the potential to influence CO_2 storage both through its influence as a "lid" on surface-ocean outgassing [17], and its impact on deep circulation [11]. Expansion of sea ice at the LGM [11], alongside an increase in surface ocean density in the Southern Ocean relative to the North Atlantic [20], would help create an expanded lower cell with salty [13], CO_2-rich water. This may shoal the upper/lower cell boundary above the zone of enhanced mixing over rough bottom topography [11,14], trapping salt and CO_2 in the abyss. Accumulation of CO_2 at depth would be further promoted by an enhanced biological pump due to iron fertilization [6] and increased upper ocean stratification, which would also reduce CO_2 escape through leads and during ice-free conditions.

This framework may also explain release of CO_2 from the deep Southern Ocean on millennial timescales [21]. CO_2 rise typically occurs during intervals of cold stadial conditions in the Northern Hemisphere and warming in the South (the bipolar seesaw) [22]. This southern warming is associated with a decrease in Southern sea ice (Figures 2, 3) and a decrease in the Southern Ocean to North Atlantic surface density gradient, shifting the boundary between the overturning cells to greater depth in the basins [11 20]. CO_2-rich water previously isolated in the abyss may thus be mixed into the upper cell over rough topography in the ocean basins, and/or transferred into the upper cell upon upwelling North of the sea ice edge, perhaps aided by the westerly winds [23,24] or increased mixed layer depths in the Southern Ocean. CO_2 loss from the deep ocean may also aided by reduced biological pump efficiency [6]. Whatever the exact mechanism, this carbon transfer is recorded by a pH increase in our lower cell corals and a pH decrease in our upper cell corals, as CO_2 is transferred to the upper ocean and the atmosphere. Note that as a southward shift in the fronts at these times might be expected to expose our sites to higher-pH water (Figure 1), the transfer of low-pH DIC-rich water into the upper cell may be even larger than observed. Indeed a southward frontal shift and breakdown in stratification likely explain the younging seen in upper cell radiocarbon [4,25] at this time (Figure S4). Upwelling of carbon and nutrient-rich water during cold Northern Hemisphere stadials is also supported by low pH in surface waters, as recorded by boron isotopes in planktic foraminifera [26], and enhanced opal fluxes [23] (Figure 3 & S4). If salt from the high salinity lower cell [13] is also transferred back into the upper cell, this may aid the re-initiation of NADW formation [27]. Once interstadial conditions are reestablished in the North Atlantic, the Southern Ocean starts to cool via the bipolar seesaw and sea ice expands [28]. This shoals the cell boundary, reduces ocean-atmosphere exchange, and allows CO_2 and salt to again become trapped in the abyss (Figure 4).

The centennial-scale CO_2 jumps at 14.7 and 11.7 ka [12], which are associated with pronounced minima in upper cell pH (Figure 3), appear to require a more efficient mode of Southern Ocean CO_2 release associated with abrupt

Northern Hemisphere warming [25]. High-resolution records of Antarctic deuterium excess indicate a northward shift in the Southern Westerly winds synchronous with abrupt Northern Hemisphere warming [29]; in contrast the bipolar seesaw cooling response in the south is lagged, with Antarctic $\delta^{18}O$ and sea salt sodium taking around 200 years to show the onset of cooling conditions and increased sea ice production [28] (Figure 3). This may lead to a transient condition in the Southern Ocean where CO_2 can be efficiently mixed up from the lower cell [24], due to the fast shift in the winds, and then outgas unimpeded by sea ice, which has not yet expanded [17]. The northward shift in the fronts might also contribute to the pH minima by exposing our upper cell sites to lower-pH water from the South (Figure 1), but such a shift would have to be large given that upper cell pH appears to reach values similar to, or even lower than, the lower cell at this time, suggesting increased input of CO_2-rich water is required. Increased input of previously isolated carbon-rich waters is also seen in radiocarbon data [4,25], which show an interruption of their deglacial younging and a slight increase in age during these events (Figure S4). Whatever the exact mechanisms involved, our data demonstrate that the Southern Ocean may fill with CO_2-rich waters on centennial timescales and may thus give out its carbon rapidly, countering suggestions that centennial-scale CO_2 jumps are too quick for a deep ocean driver and require exogenous carbon addition (such as from methane hydrates or the terrestrial biosphere [30]). Our data show that rapid changes in the Southern Ocean acted in concert with strong AMOC resumption [25] to drive rapid CO_2 rise.

Although our lower cell $\delta^{11}B$-pH data generally show a close coupling with atmospheric CO_2, this relationship is somewhat muted during peak glacial conditions, with pronounced minima in pH at ~26 and 20 ka, alongside extensive sea ice [28], low upwelling [23], and an efficient biological pump [6] (Figure S3), but minimal change in atmospheric CO_2. This supports the idea of a lower limit on atmospheric CO_2 at ~190 ppm [31]: although Southern Ocean carbon storage continues to increase, its influence on the atmosphere

193 appears to be offset by other processes, perhaps the onset of CO_2 limitation
194 on primary productivity on land [31].

195

196 Overall, our data provide a clear demonstration that storage and release of
197 CO_2 in the deep Southern Ocean plays a central role in glacial-interglacial
198 atmospheric CO_2 change. These changes in ocean CO_2 storage were likely
199 driven by a combination of changes in ocean circulation, biological pump
200 efficiency, and sea ice cover. We note a close correspondence between CO_2
201 storage and ice core sea ice sodium records, which may suggest that
202 Southern Ocean sea ice plays a key role, due to its joint influence on deep
203 overturning and surface outgassing. This provides a mechanistic explanation
204 for the tight link between Antarctic temperature and CO_2 change on glacial-
205 interglacial timescales, though several processes acting together are likely
206 required to explain the full magnitude of glacial CO_2 change. Our data also
207 highlight the ability of the Southern Ocean – and its CO_2 – to respond to
208 millennial and centennial-scale shifts in climate linked to the North Atlantic's
209 overturning circulation. Indeed, it is possible that the framework presented
210 here, which links the storage and release of deep ocean CO_2 and salt to
211 changes in Southern Ocean sea ice and the bipolar seesaw, may help
212 account for the occurrence of millennial-scale CO_2 and climate change during
213 mid-glacial conditions. At these times, moderate sea ice extent means that
214 the boundary between the ocean's lower and upper cells is located near the
215 top of rough seafloor topography. Small shifts in the cell boundary, linked to
216 changes in the Southern sea ice edge, may thus drive large shifts in the
217 degree of mixing between the lower and upper cells, and their salt and CO_2.
218 This framework may also give behavior similar to "density oscillator" models
219 for rapid climate change [27,32,33]: when AMOC is active and the Northern
220 Hemisphere warms, the South cools and sea ice expands, progressively
221 isolating cold salty water (and CO_2) in the lower cell. This may make the
222 AMOC vulnerable to collapse, at which point the South warms, sea ice
223 retreats, and the cell-boundary deepens. This helps mix salt (and CO_2) back
224 into the upper cell and makes the lower cell fresher and warmer, reducing the

225 deep ocean density contrast, and helping poise the system for AMOC
226 resumption.
227

References

1. Broecker, W. S. Glacial to interglacial changes in ocean chemistry. *Progress in Oceanography* **11,** 151–197 (1982).
2. Sarmiento, J. L. & Toggweiler, J. R. A new model for the role of the oceans in determining atmospheric pCO_2. *Nature* **308,** 621–624 (1984).
3. Sigman, D. M., Hain, M. P. & Haug, G. H. The polar ocean and glacial cycles in atmospheric CO_2 concentration. *Nature* **466,** 47–55 (2010).
4. Burke, A. & Robinson, L. F. The Southern Ocean's Role in Carbon Exchange During the Last Deglaciation. *Science* **335,** 557–561 (2012).
5. Roberts, J. *et al.* Evolution of South Atlantic density and chemical stratification across the last deglaciation. *PNAS* 201511252–14 (2016). doi:10.1073/pnas.1511252113
6. Martinez-Garcia, A. *et al.* Iron Fertilization of the Subantarctic Ocean During the Last Ice Age. *Science* **343,** 1347–1350 (2014).
7. Yu, J. *et al.* Deep South Atlantic carbonate chemistry and increased interocean deep water exchange during last deglaciation. *Quaternary Science Reviews* **90,** 80–89 (2014).
8. Rae, J. W. B. *et al.* Deep water formation in the North Pacific and deglacial CO2 rise. *Paleoceanography* **29,** 645–667 (2014).
9. Yu, J. *et al.* Responses of the deep ocean carbonate system to carbon reorganization during the Last Glacial--interglacial cycle. *Quaternary Science Reviews* **76,** 39–52 (2013).
10. Rickaby, R. E. M., Elderfield, H., Roberts, N., Hillenbrand, C. D. & Mackensen, A. Evidence for elevated alkalinity in the glacial Southern Ocean. *Paleoceanography* **25,** PA1209 (2010).
11. Ferrari, R. *et al.* Antarctic sea ice control on ocean circulation in present and glacial climates. *PNAS* **111,** 8753–8758 (2014).
12. Marcott, S. A. *et al.* Centennial-scale changes in the global carbon cycle during the last deglaciation. **514,** 616–619 (2014).
13. Adkins, J. F., McIntyre, K. & Schrag, D. P. The salinity, temperature, and $\delta^{18}O$ of the glacial deep ocean. *Science* **298,** 1769–1773 (2002).
14. Burke, A., Stewart, A. L., Adkins, J. F. & Ferrari, R. The glacial mid-depth radiocarbon bulge and its implications for the overturning circulation. *Paleoceanography* **30,** 1021–1039 (2015).
15. Charles, C. D. *et al.* Millennial scale evolution of the Southern Ocean chemical divide. *Quaternary Science Reviews* **29,** 399–409 (2010).
16. Jaccard, S. L., Galbraith, E. D., Martinez-Garcia, A. & Anderson, R. F. Covariation of deep Southern Ocean oxygenation and atmospheric CO_2 through the last ice age. *Nature* **530,** 207–210 (2016).
17. Stephens, B. B. & Keeling, R. F. The influence of Antarctic sea ice on glacial-interglacial CO_2 variations. *Nature* **404,** 171–174 (2000).
18. Wolff, E. W. *et al.* Southern Ocean sea-ice extent, productivity and iron flux over the past eight glacial cycles. *Nature* **440,** 491–496 (2006).
19. Abram, N. J., Wolff, E. W. & Curran, M. A. J. A review of sea ice proxy information from polar ice cores. *Quaternary Science Reviews* **79,** 168–183 (2013).
20. Galbraith, E. & de Lavergne, C. Response of a comprehensive climate

model to a broad range of external forcings: relevance for deep ocean ventilation and the development of late Cenozoic ice ages. *Climate Dynamics* 1–27 (2018). doi:10.1007/s00382-018-4157-8
21. Ahn, J. & Brook, E. J. Atmospheric CO_2 and Climate on Millennial Time Scales During the Last Glacial Period. *Science* **322,** 83–85 (2008).
22. Stocker, T. F. The seesaw effect. *Science* (1998).
23. Anderson, R. F. *et al.* Wind-Driven Upwelling in the Southern Ocean and the Deglacial Rise in Atmospheric CO_2. *Science* **323,** 1443–1448 (2009).
24. Abernathey, R. & Ferreira, D. Southern Ocean isopycnal mixing and ventilation changes driven by winds. *Geophysical Research Letters* **42,** 10,357–10,365 (2015).
25. Chen, T. *et al.* Synchronous centennial abrupt events in the ocean and atmosphere during the last deglaciation. *Science* **349,** 1537–1541 (2015).
26. Martínez-Botí, M. A. *et al.* Boron isotope evidence for oceanic carbon dioxide leakage during the last deglaciation. *Nature* **518,** 219–222 (2015).
27. Broecker, W. S., Bond, G., Klas, M., Bonani, G. & Wolfli, W. A salt oscillator in the glacial Atlantic? 1. The concept. *Paleoceanography* **5,** 469–477 (1990).
28. Members, W. D. P. *et al.* Precise interpolar phasing of abrupt climate change during the last ice age. *Nature Publishing Group* **520,** 661–16 (2015).
29. Markle, B. R. *et al.* Global atmospheric teleconnections during Dansgaard-Oeschger events. *Nature Geoscience* **10,** 36–40 (2017).
30. Köhler, P., Knorr, G. & Bard, E. Permafrost thawing as a possible source of abrupt carbon release at the onset of the Bølling/Allerød. *Nature Communications* **5,** 1–10 (2014).
31. Galbraith, E. D. & Eggleston, S. A lower limit to atmospheric CO_2 concentrations over the past 800,000 years. *Nature Geosci* **10,** 295–298 (2017).
32. Bereiter, B., Shackleton, S., Baggenstos, D., Kawamura, K. & Severinghaus, J. Mean global ocean temperatures during the last glacial transition. *Nature Publishing Group* **553,** 39–44 (2018).
33. Keeling, R. F. & Stephens, B. B. Antarctic sea ice and the control of Pleistocene climate instability. *Paleoceanography* (2001).

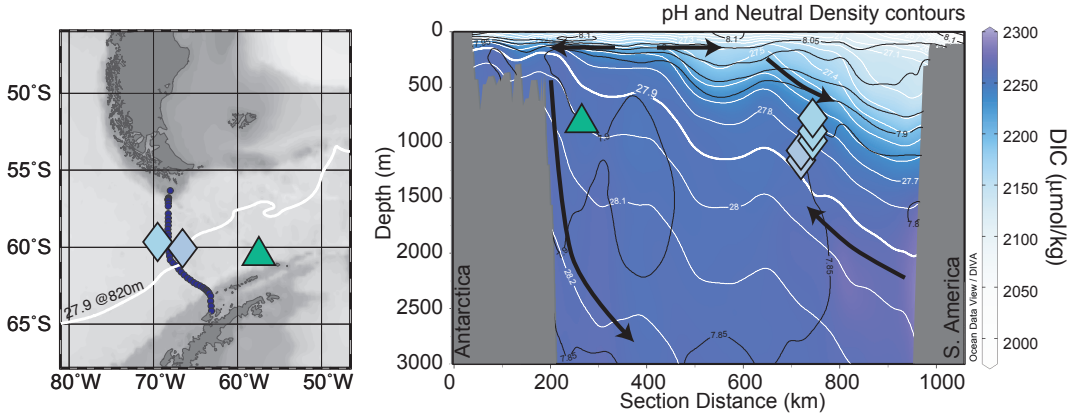

Figure 1: Locations of deep-sea coral samples. The cross section (right panel) is constructed from hydrographic stations across the Drake Passage (dark blue dots on map, left panel). Steeply dipping isopycnals in this region (white contours) mean our sites fall into two groups spanning distinct volumes of the deep ocean [11]. The green triangle marks the lower cell sites, which lie close to the Antarctic continental margin in the Shackleton Fracture Zone; the blue diamonds the upper cell sites, which lie at lower densities on the Sars (lighter blue) and Interim (darker blue) seamounts. Lower cell waters are rich in DIC (shading, right panel) with low pH (black contours); upper cell waters have higher pH and are more closely connected to the atmosphere. Coral locations on the section are given in coordinates of depth and neutral density, based on CTD data collected alongside the coral dredges. Note that there is no significant offset in our $\delta^{11}B$ data between upper cell corals from different depths (Figure S2), and that differences in pH between these sites are small compared to the range seen in our records. The 27.9 neutral density contour in the map view (left) is shown at 820 m, the average depth of our corals. Section data are from GLODAPv2 [34,35], plotted using isopycnal gridding in Ocean Data View.

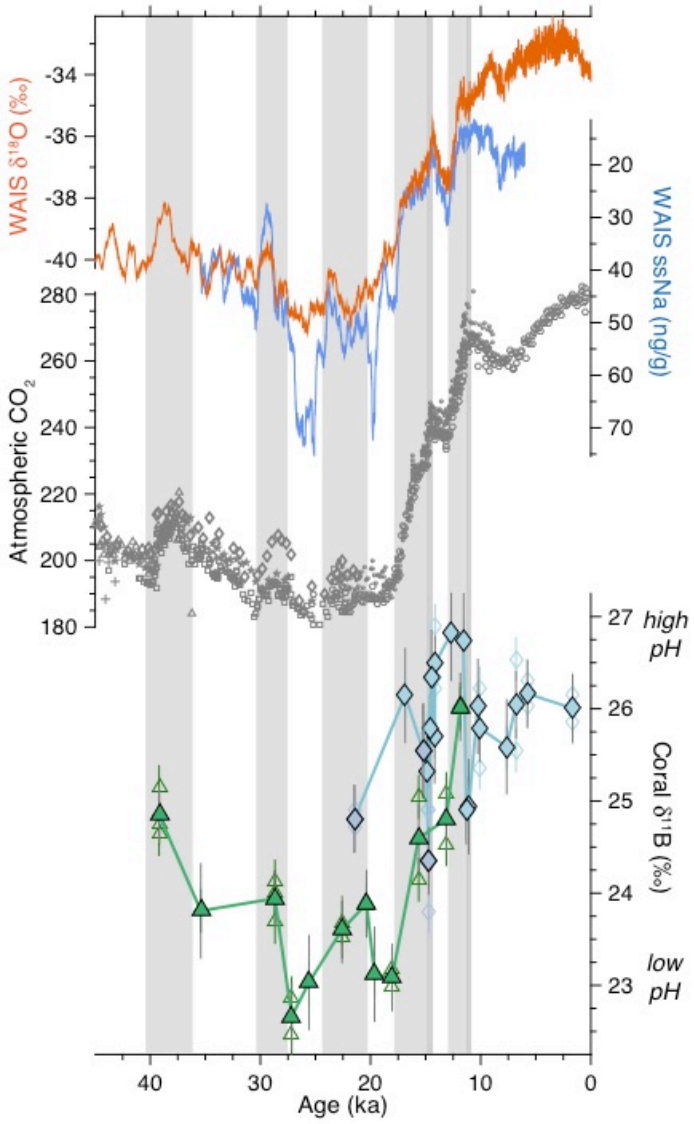

335

336 **Figure 2: Deep Southern Ocean CO_2 chemistry, atmospheric CO_2, and**
337 **Antarctic climate records over the last 40,000 years.** Green triangles and
338 blue diamonds show lower and upper cell deep-sea coral $\delta^{11}B$ data
339 respectively. Individual subsamples are shown in small open symbols and
340 mean values in larger filled symbols. Error bars on individual subsamples are
341 equivalent to 2 SD analytical reproducibility and error bars on mean coral
342 values represent 2 SE uncertainty on the mean of replicate subsamples (see
343 Methods). Synchronised ice core CO_2 data [36] are shown in grey symbols:
344 circles from Dome C, dots from WAIS, stars from Taylor Dome, triangles from
345 TALDICE, pluses from EDML, diamonds from Byrd, and squares from Siple
346 Dome. WAIS $\delta^{18}O$ (orange line), which reflects Antarctic temperature, and
347 sea salt sodium (blue line), a proxy for sea ice, have been smoothed with a
348 running mean [28]. Grey bands highlight intervals of CO_2 rise.

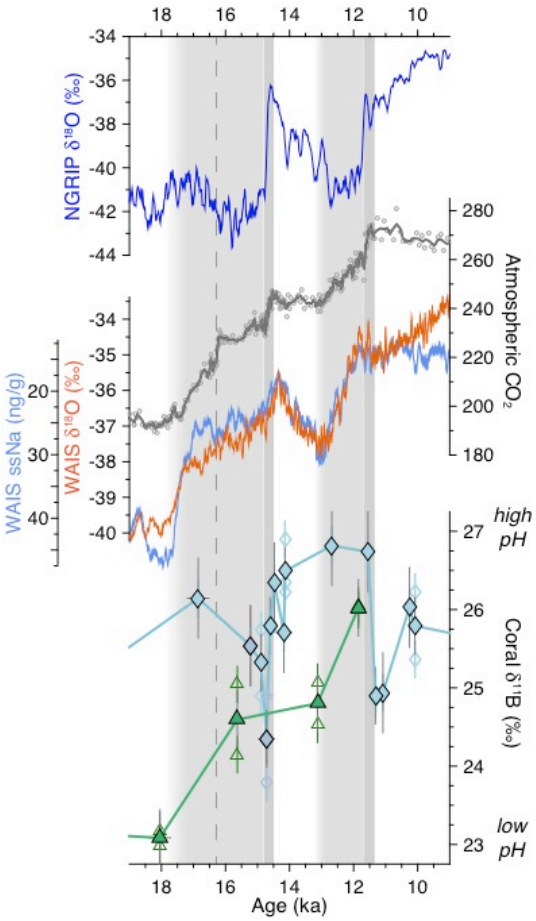

Figure 3: Deglacial records of deep Southern Ocean CO_2 chemistry, atmospheric CO_2, and climate over Antarctica and Greenland. Green triangles and blue diamonds show lower and upper cell deep-sea coral $\delta^{11}B$ data respectively. Individual subsamples are shown in small open symbols and mean values in larger filled symbols. Error bars on individual subsamples are equivalent to 2 SD analytical reproducibility and error bars on mean coral values represent 2 SE uncertainty on the mean of replicate subsamples (see Methods). Greenland ice core $\delta^{18}O$ (dark blue line), WAIS $\delta^{18}O$ (orange line), and sea salt sodium (blue line), have been smoothed with a running mean [28]. CO_2 data (grey symbols) are from WAIS [12] with a 5-point running mean (grey line). Light grey vertical bands highlight intervals of millennial-scale CO_2 rise; dark grey vertical bands highlight intervals of centennial-scale CO_2 rise associated with North Hemisphere warming, and the vertical dashed line indicates the rapid CO_2 rise event that occurs at 16.3 ka, within Heinrich Stadial 1.

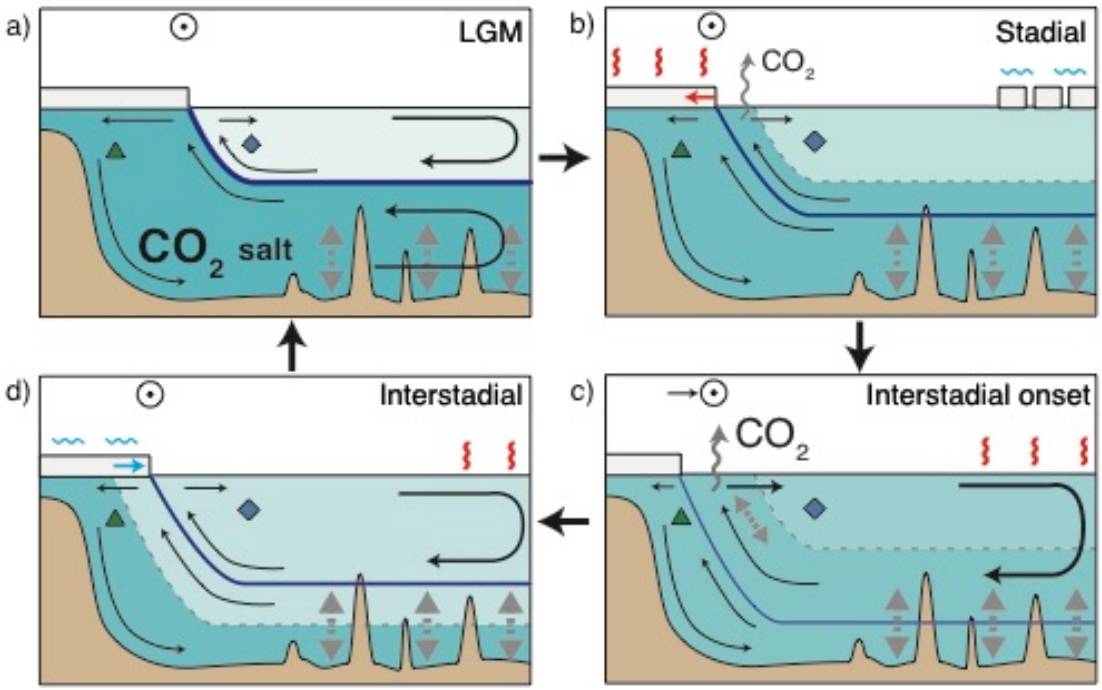

Figure 4

a) At the LGM extensive Southern Ocean sea ice creates an expanded lower cell with salty, CO_2-rich water. The cell boundary is shoaled above the zone of enhanced mixing over rough bottom topography, isolating salt and CO_2 in the abyss.

b) During a Northern Hemisphere stadial event, North Atlantic overturning is reduced, the Southern Ocean warms, and sea ice retreats. This shifts the cell boundary such that water previously isolated in the lower cell now upwells North of the sea ice edge. This water – and its CO_2 and salt – are transferred to the upper ocean and CO_2 outgases to the atmosphere. Transfer of salt from the lower to the upper cell may help re-initiate NADW formation.

c) At the onset of a Northern Hemisphere interstadial event (e.g. Bølling-Allerød, end Younger Dryas), resumption of NADW warms the Northern Hemisphere and leads to a rapid Northward shift in the Westerly winds; the Southern Ocean temperature and sea ice response is slower. This creates a transient condition where sea ice is unable to shield the ocean from enhanced isopycnal mixing nor the atmosphere from enhanced outgassing, leading to centennial-scale CO_2 rise.

d) As the interstadial continues, the Southern Ocean cools and sea ice expands. This shoals the cell boundary and allows salt and carbon to again become trapped in the abyss.

Climate states with moderate sea ice extent, where the cell boundary hovers around the top of rough seafloor topography, may give favourable conditions for rapid climate and CO_2 change, as the ocean flips between modes of connection vs isolation of the upper and lower cells.

398 **Acknowledgements**

399 This work was supported by NERC Standard Grant NE/N003861/1 to
400 J.W.B.R. and L.F.R., a NOAA Climate and Global Change VSP Fellowship to
401 J.W.B.R, NERC Standard Grant NE/M004619/1 to AB and JWBR, a NERC
402 Strategic Environmental Science Capital Grant to A.B. and J.W.B.R., Marie
403 Curie Career Integration Grant CIG14-631752 to AB, an ERC consolidator
404 grant to L.F.R., NSF grant OCE-1503129 to J.F.A., and NERC studentships to
405 B.T. and E.L. We thank 3 anonymous reviewers for comments that
406 substantially improved this manuscript.

407

408 **Author Contributions**

409 J.W.B.R., A.B., and L.F.R. designed the study. A.B., L.F.R., T.C., and T.L.
410 collected and uranium-thorium dated the coral samples. J.W.B.R., B.T., E.L.,
411 C.C., J.S., and D.C.N. made boron isotope analyses. All authors contributed
412 to the interpretation and the preparation of the manuscript.

413

414 The authors declare no competing interests.

415 Correspondence and requests for materials should be addressed to J.W.B.R
416 (jwbr@st-andrews.ac.uk)

417

Methods

Sample collection and chronology

Deep-sea coral samples were collected by dredge during two cruises in the Drake Passage (NBP0805 and NBP1103). A total of 392 *D. dianthus* samples were initially "reconnaissance" dated, either by ^{14}C [37,38] or laser ablation U-Th [25,39], to obtain preliminary ages. Suitable samples with ages within the last ~50 ka were then precisely dated by isotope dilution U-Th by MC-ICPMS [4,25]. All ages have been published previously, and have typical uncertainties of around ±1 % (2 SD), though this varies between samples depending on their initial ^{230}Th (calculated from measured ^{232}Th and assuming an initial atomic $^{232}Th/^{230}Th$ ratio of 12,500 ± 12,500). Age errors are plotted in all time series figures but are typically smaller than the symbols. This precisely-dated and unbioturbated deep sea archive provides a unique record of ocean pH change at resolution comparable to the ice cores.

Sample preparation

Coral pieces were sampled from the growing tip of coral septa. Samples were physically cleaned using a Dremmel tool to remove all visible iron-manganese oxides and any chalky white carbonate, indicative of alteration.

We tested the potential influence of microstructural variability on coral $\delta^{11}B$ with multiple solid sub-samples from the same coral (Figure S6). Coral centres of calcification have previously been observed to have anomalously light boron isotope values, along with high Mg/Ca and low U/Ca [40-44], and we observe this same coupled variability in our coral subsamples (Figure S6). However this microstructural signal is typically small compared to the size of the boron isotope signals seen in our record. We had expected the smaller subsamples to exhibit more scatter, due to the potential influence of coral centers of calcification (COCs), but this is not shown in these data. There is in fact slightly more variability between larger chunks, perhaps due to the increased chance of sampling some COC material. For our records we used

coral pieces of ~1 mg. We also mitigated microstructural influences by taking multiple solid subsamples from each coral when possible (shown as open symbols). Two subsamples (at 1.6 ka and 20.4 ka) were rejected from our total set of 55 as having anomalous $\delta^{11}B$ values (~1 ‰ lighter than the mean of 3-4 other subsamples from that coral), which may be due to the impact of COC material.

Boron isotope analysis

Solid coral samples were crushed to a grain size <1 mm using an agate pestle and mortar. Samples were then subjected to oxidative cleaning to remove organic matter following established protocols [45-48], using warm 1 % hydrogen peroxide, buffered in 0.1 M NH_4OH, followed by leaching in 0.0001 M HNO_3, and dissolution in 0.075 M distilled HNO_3. Boron was purified from the sample matrix using column chromatography with the boron-specific ion exchange resin Amberlite 743 [49-51].

Boron isotope composition was analysed by MC-ICPMS by sample-standard bracketing [47,48,51]. Early analyses used NH_3 to improve boron washout in the spray chamber [52], which reduces background signals to ~3 % of the preceding sample within ~3 minutes [51]. More recent analyses used dilute HF [53], which reduces background signals to ~0.5 % within ~3 minutes. In contrast to some previous work, where samples are analysed in pure 0.3 M HF [53], we add a small volume of concentrated HF to our sample following column elution in 0.5 M HNO_3, giving a solution of 0.5 M HNO_3 + 0.3 M HF. Similarly, bracketing standards (NIST 951) and instrument blank acid were analysed in 0.5 M HNO_3 + 0.3 M HF to ensure consistent mass bias and blank corrections, though beyond improved washout we do not find any significant influence of HF concentration: boric acid standards run as dummy-samples run with HF concentrations from 0 to 0.5 M HF bracketed against 951 in 0.5 M HNO_3 + 0.3 M HF all yield identical boron isotope ratios. Carbonate standards (JCP, NIST RM8301C) passed through columns and run with NH_3 or HF also yield identical values.

All preparation and analytical work was carried out in boron-free clean laboratory conditions. Over the course of this work samples were analysed at the University of Bristol and Caltech on a Neptune MC-ICPMS, and the University of St Andrews on a Neptune Plus MC-ICPMS, though in all cases following nearly identical protocols. Each of these laboratories has taken part in published and ongoing inter-laboratory comparison studies [48] and there is no analytical offset between samples run in these laboratories.

Long-term analytical reproducibility on $\delta^{11}B$ measurements in these laboratories (assessed with carbonate standards given the same treatment as samples) is around 0.23 ‰ (2 SD) on samples of the size used here (~20 ng boron) – this is the error bar given on individual subsamples (open symbols in figures). We use a more conservative uncertainty for our mean coral $\delta^{11}B$ values (filled symbols in figures), to account for the $\delta^{11}B$ variability between subsamples from the same coral. This is based on the pooled standard deviation of the replicate samples in our records and in Figure S6 (2 SD = 0.51 ‰). Uncertainty is reduced on mean values with multiple replicates (n), which is accounted for using the standard error (SD/$\sqrt{n}$).

$\delta^{11}B$ and pH in deep-sea corals

The boron isotope pH proxy provides a sensitive measure of the ocean carbonate system, though in common with many proxies, is also influenced by modification during biomineralisation [54-57]. In particular, coral $\delta^{11}B$ is influenced by internal pH-elevation during biomineralisation [58,59], which may buffer its sensitivity to external seawater pH changes in some settings. To examine this we have compiled modern *D. dianthus* $\delta^{11}B$ calibration data [44,56,60] from water depths >100 m, and have added two recent Southern Ocean samples. This indicates that the relationship between seawater pH and coral $\delta^{11}B$ is curved, with $\delta^{11}B$ becoming more sensitive to external seawater at lower pH (Figure S5). This suggests that corals find it harder to elevate internal pH as external conditions become more acidic, which is reasonable, given the increase in energy demand required for additional proton expulsion [61]. It also means that corals are likely to be more sensitive to

external pH conditions at lower pH sites, such as the Southern Ocean locations in this study. Hence, the pH changes that occured during the last 40,000 yr are evident as large, easily resolvable changes in $\delta^{11}B$ in our coral record.

Reconstructed pH based on this calibration is shown in Figure S1. Given the paucity of modern deep-sea coral samples from low-pH waters, our record extends beyond the available calibration range. As a result conversion to absolute pH values carries relatively large uncertainty, which is hard to assess. We thus prefer to focus on relative changes in the $\delta^{11}B$ records themselves, which provide a proxy of carbonate chemistry in their own right [62], analogous to the typical use of $\delta^{18}O$ records in paleoceanography.

Data availability

The data produced in this study is available as a supplementary table and will also be made available at the NOAA and Pangaea data repositories.

Supplementary Figures

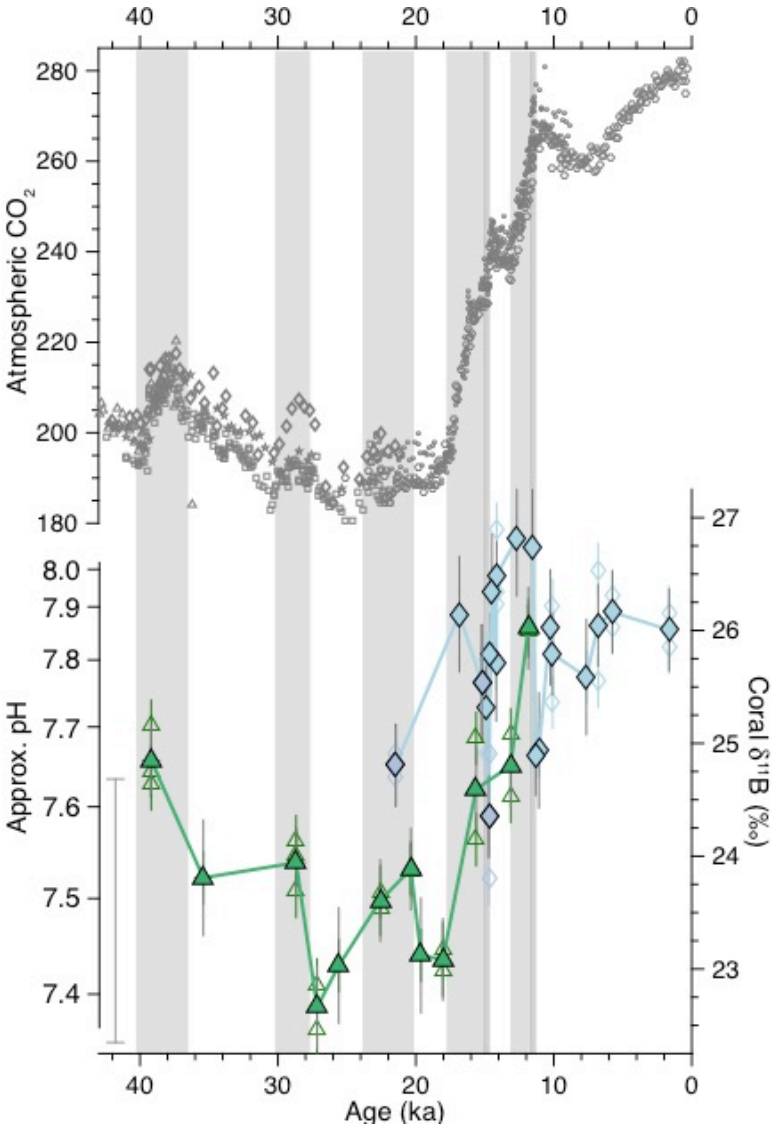

Figure S1: Deep Southern Ocean CO_2 chemistry and atmospheric CO_2 over the last 40,000 years. Green triangles and blue diamonds show lower and upper cell deep-sea coral $\delta^{11}B$ data respectively. Individual subsamples are shown in small open symbols and mean values in larger filled symbols. Error bars on individual subsamples are equivalent to 2 SD analytical reproducibility and error bars on mean coral values represent 2 SE uncertainty on the mean of replicate subsamples (see Methods). Approximate pH values are given based on coral $\delta^{11}B$ using the calibration in Figure S5, but uncertainty on this calibration is large (inset error bar), given the paucity of modern deep-sea coral data from low pH waters. Instead we focus on the $\delta^{11}B$ values themselves, which provide a proxy of carbonate chemistry in their own right [62]. Synchronised ice core CO_2 data [36] are shown in grey symbols: circles from Dome C, dots from WAIS, stars from Taylor Dome, triangles from TALDICE, pluses from EDML, diamonds from Byrd, and squares from Siple Dome. Grey bands highlight intervals of CO_2 rise.

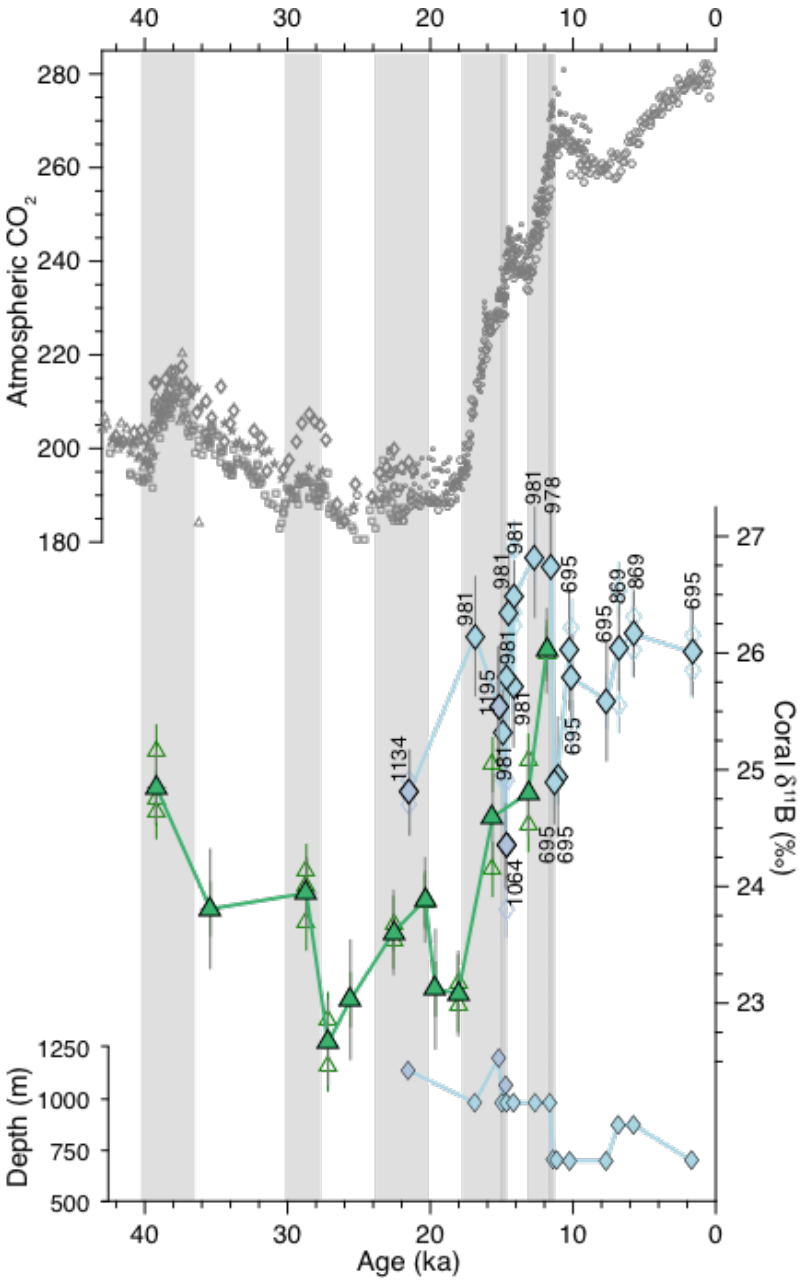

Figure S2: Deep Southern Ocean CO_2 chemistry and atmospheric CO_2 over the last 40,000 years, highlighting the depths of upper cell corals. Symbols and data are as plotted in Figure S1, but with the addition of the lower panel and annotations showing the depth in meters of each upper cell coral sample. No systematic offset is seen between samples from different depths. The only signal that occurs simultaneous with a change in depth is the decrease at ~11.5 ka, but the jump back up to higher $\delta^{11}B$ values following this event occurs without a change in depth, giving confidence that the excursion is not a depth-related signal. Furthermore the large excursion at ~14.7 ka occurs without a significant change in depth. Note that all of the lower cell corals come from within 17 m water depth of each other.

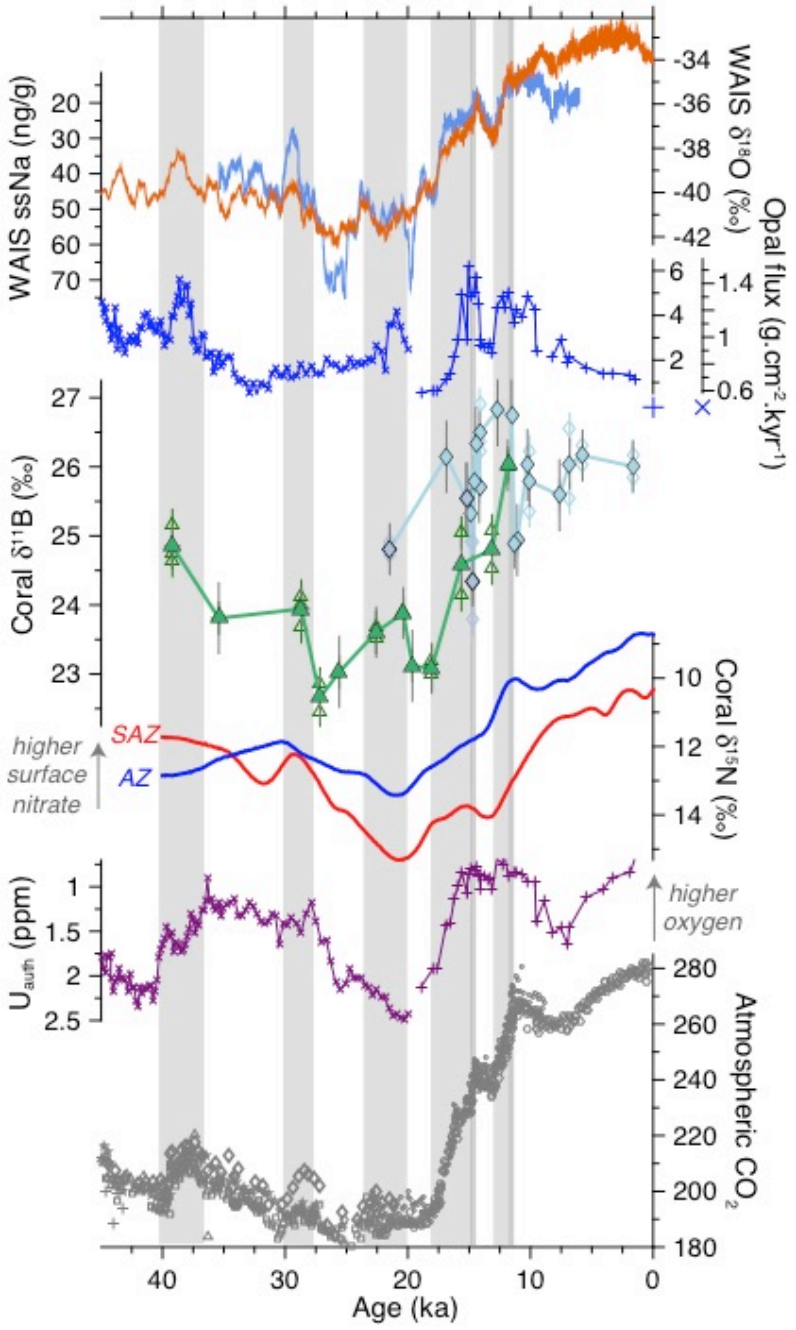

Figure S3: Records of Southern Ocean biogeochemistry and CO_2 over the last 40,000 yr. Data are plotted as in Figure 2, but with opal flux [23], a proxy for upwelling, deep sea coral $\delta^{15}N$ [63], a proxy for surface ocean nitrate consumption, and authigenic uranium concentrations [16], a proxy for bottom water redox. The opal flux and authigenic uranium records combine two sediment cores: TN057-13-4PC in the younger part of the record (pluses) and TN057-14PC in the older part of the record (crosses). The opal flux records from each core are shown on separate scales. The coral $\delta^{15}N$ data are grouped into samples from the Antarctic Zone (AZ, blue) and Subantarctic Zone (SAZ, red). Smoothed fits to the data are shown, as provided in the original study [63]. Intervals of low CO_2 during the last ice age are associated with low upwelling, an efficient biological pump, low oxygen water rich in respired carbon, and low-pH carbon-rich water in the deep Southern Ocean.

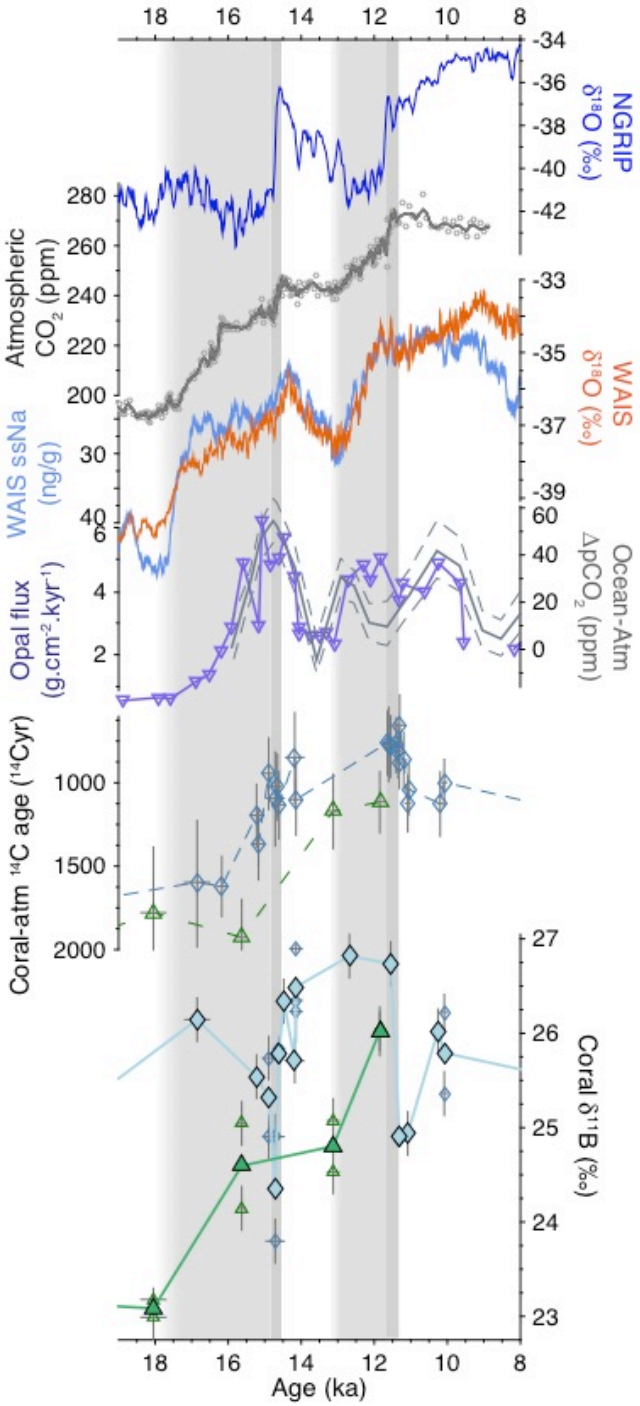

Figure S4: Deglacial records of Southern Ocean CO_2 chemistry and opal fluxes, and climate over Antarctica and Greenland. Data are plotted as in Figures 2 and 3, but with opal flux [23], a proxy for upwelling, surface ocean-atmosphere CO_2 difference, based on $\delta^{11}B$ in planktic foraminifera [26], and radiocarbon data [4,25] from corals within these sample groupings, shown as age offsets compared to the contemporaneous atmosphere. Intervals of rising CO_2 in the atmosphere are associated with input of waters rich in CO_2 and nutrients to the upper reaches of the Southern Ocean. Radiocarbon ages reflect the competing influences of upwelling of ^{14}C-depleted waters and improved ventilation over the deglaciation.

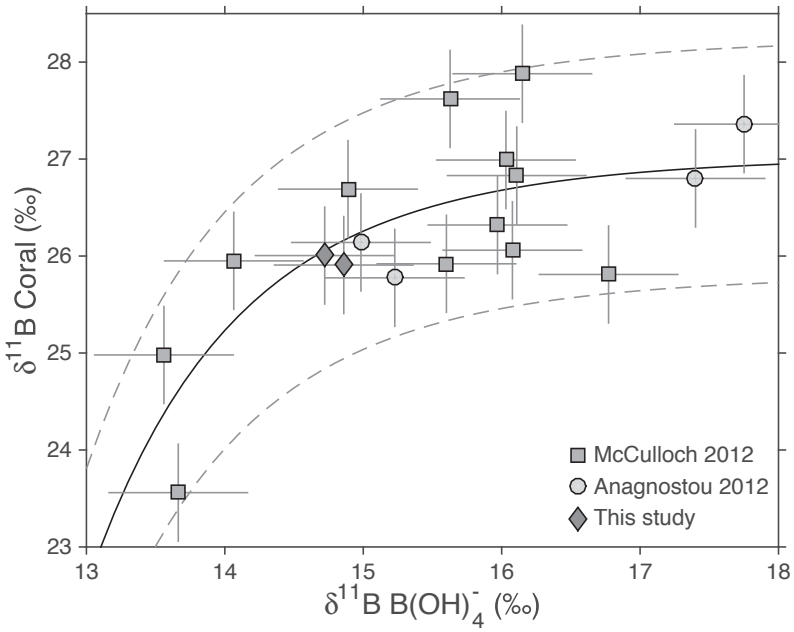

Figure S5: Boron isotope calibration for modern *D. dianthus*. Data are from open ocean sites in [44,56,60], with two additional recent (<1650 yr) samples from the Southern Ocean from this study. Water column $\delta^{11}B$ of borate ($B(OH)_4^-$) values are as previously published or are calculated from carbonate chemistry data from nearby GLODAPv2 sites for the new samples, following [47,62]. Note that the sensitivity of $\delta^{11}B$ in carbonates to pH is based on the pH sensitivity of $\delta^{11}B$ of borate. pH itself is not easily shown on a plot like this, as the relationship between $\delta^{11}B$ of borate and pH is also somewhat influenced by water temperature, salinity, and depth. A power law function was fitted to the data using Matlab's curve fitting toolbox (solid line: $\delta^{11}B_{Coral} = -1.82^{14} \times \delta^{11}B_{B(OH)4-}{}^{-12.22} + 27.03$; $R^2 = 0.57$). Dashed lines show the 95 % confidence intervals and give a measure of calibration uncertainty as shown in the error bar in Figure S1, though data from a given site may be able to record relative changes in pH more sensitively, as seen in many paleo-proxies.

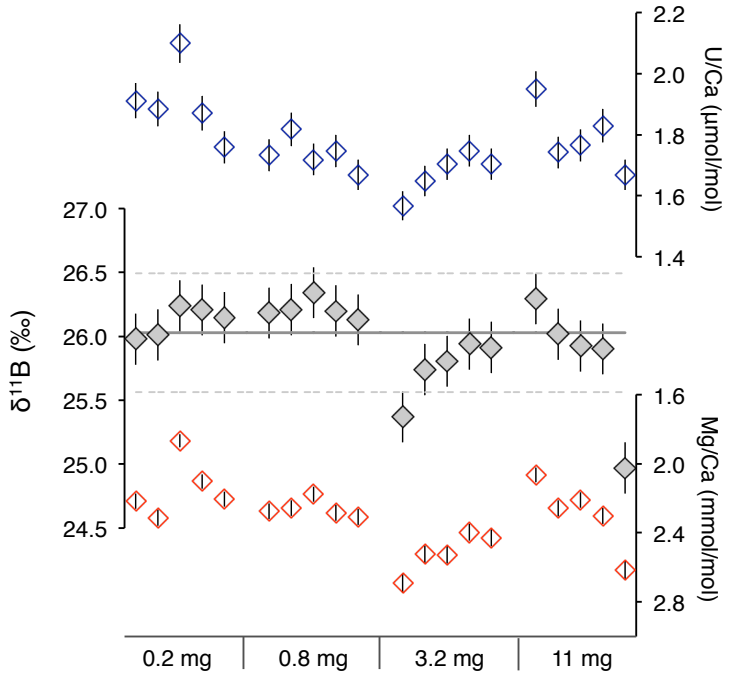

Figure S6: Replicate subsamples from a *D. dianthus* septum. To test for the potential influence of microstructural variability in composition, a coral septum was divided into 4 areas, which were then split into chunks of approximately 0.2, 0.8, 3.2 and 11 mg respectively. These were then individually crushed, cleaned, and analysed. This sample treatment was designed to preserve heterogeneity between subsamples, though note that the clustering of subsamples of a given size from a certain area of the coral may lead to that group recording a slightly different signal (as seen in the 3.2 mg group). The lines in the middle panel show the mean and 2 SD, excluding one outlier in the 11 mg group. $\delta^{11}B$ is correlated with Mg/Ca and U/Ca, showing the influence of internal variability in coral composition.

Additional References

34. Key, R. M. *et al.* Global Ocean Data Analysis Project, Version 2 (GLODAPv2). *EPIC3ORNL/CDIAC-162, NDP-093, Carbon Dioxide Information Analysis Center, Oak Ridge Nat Lab* (2015). doi:10.3334/CDIAC/OTG
35. Olsen, A. *et al.* The Global Ocean Data Analysis Project version 2 (GLODAPv2) – an internally consistent data product for the world ocean. *Earth System Science Data* **8,** 297–323 (2016).
36. Bereiter, B. *et al.* Revision of the EPICA Dome C CO_2 record from 800 to 600 kyr before present. *GRL* **42,** 542–549 (2015).
37. Burke, A. *et al.* Reconnaissance dating: A new radiocarbon method applied to assessing the temporal distribution of Southern Ocean deep-sea corals. *Deep Sea Research Part I: Oceanographic Research Papers* **57,** 1510–1520 (2010).
38. Margolin, A. R. *et al.* Temporal and spatial distributions of cold-water corals in the Drake Passage: Insights from the last 35,000 years. *Deep Sea Research Part II: Topical Studies in Oceanography* **99,** 237–248 (2014).
39. Spooner, P. T., Chen, T., Robinson, L. F. & Coath, C. Rapid uranium-series age screening of carbonates by laser ablation mass spectrometry. *Quaternary Geochronology* **31,** 28–39 (2016).
40. Sinclair, D. J., Kinsley, L. P. & McCulloch, M. T. High resolution analysis of trace elements in corals by laser ablation ICP-MS. *Geochim. Cosmochim. Acta* **62,** 1889–1901 (1998).
41. Robinson, L. F. *et al.* Primary U distribution in scleractinian corals and its implications for U series dating. *Geochem. Geophys. Geosyst. (G3)* **7,** Q05022 (2006).
42. Gagnon, A. C., Adkins, J. F., Fernandez, D. P. & Robinson, L. F. Sr/Ca and Mg/Ca vital effects correlated with skeletal architecture in a scleractinian deep-sea coral and the role of Rayleigh fractionation. *EPSL* **261,** 280–295 (2007).
43. Rollion-Bard, C., Chaussidon, M. & France-Lanord, C. Biological control of internal pH in scleractinian corals: Implications on paleo-pH and paleo-temperature reconstructions. *Comptes rendus - Geoscience* **343,** 397–405 (2011).
44. Stewart, J. A., Anagnostou, E. & Foster, G. L. An improved boron isotope pH proxy calibration for the deep-sea coral *Desmophyllum dianthus* through sub-sampling of fibrous aragonite. *Chemical geology* **447,** 148–160 (2016).
45. Boyle, E. A. Cadmium, zinc, copper, and barium in foraminifera tests. *EPSL* **53,** 11–35 (1981).
46. Barker, S., Greaves, M. & Elderfield, H. A study of cleaning procedures used for foraminiferal Mg/Ca paleothermometry. *Geochem. Geophys. Geosyst.* **4,** 8407 (2003).
47. Rae, J. W. B., Foster, G. L., Schmidt, D. N. & Elliott, T. Boron isotopes and B/Ca in benthic foraminifera: Proxies for the deep ocean carbonate system. *EPSL* **302,** 403–413 (2011).

48. Foster, G. L. *et al.* Interlaboratory comparison of boron isotope analyses of boric acid, seawater and marine $CaCO_3$ by MC-ICPMS and NTIMS. *Chem. Geol.* **358,** 1–14 (2013).
49. Kiss, E. Ion-exchange separation and spectrophotometric determination of boron in geological materials. *Analytica Chimica Acta* **211,** 243–256 (1988).
50. Lemarchand, D., Gaillardet, J., Göpel, C. & Manhès, G. An optimized procedure for boron separation and mass spectrometry analysis for river samples. *Chemical geology* **182,** 323–334 (2002).
51. Foster, G. L. Seawater pH, pCO_2 and $[CO_3^{=}]$ variations in the Caribbean Sea over the last 130 kyr: A boron isotope and B/Ca study of planktic foraminifera. *EPSL* **271,** 254–266 (2008).
52. Al-Ammar, A. S., Gupta, R. K. & Barnes, R. M. Elimination of boron memory effect in inductively coupled plasma-mass spectrometry by ammonia gas injection into the spray chamber during analysis. *Spectrochimica Acta Part B: Atomic Spectroscopy* **55,** 629–635 (2000).
53. Misra, S., Owen, R., Kerr, J. & Greaves, M. Determination of $\delta^{11}B$ by HR-ICP-MS from mass limited samples: Application to natural carbonates and water samples. *Geochemica et Cosmochimica Acta* **140,** 531–552 (2014).
54. Rae, J. W. B. in *Boron Isotopes* 107–143 (Springer, 2018).
55. McCulloch, M. T. *et al.* in *Boron Isotopes* 145–162 (Springer, 2018).
56. Anagnostou, E., Huang, K. F., You, C. F., Sikes, E. L. & Sherrell, R. M. Evaluation of boron isotope ratio as a pH proxy in the deep sea coral *Desmophyllum dianthus*: Evidence of physiological pH adjustment. *EPSL* **349-350,** 251–260 (2012).
57. Trotter, J. *et al.* Quantifying the pH `vital effect' in the temperate zooxanthellate coral Cladocora caespitosa: Validation of the boron seawater pH proxy. *EPSL* **303,** 163–173 (2011).
58. Venn, A. A. *et al.* Impact of seawater acidification on pH at the tissue-skeleton interface and calcification in reef corals. *PNAS* **110,** 1634–1639 (2013).
59. Allison, N., Cohen, I., Finch, A. A., Erez, J. & Tudhope, A. W. Corals concentrate dissolved inorganic carbon to facilitate calcification. *Nature Communications* **5,** 5741 (2014).
60. McCulloch, M. *et al.* Resilience of cold-water scleractinian corals to ocean acidification: Boron isotopic systematics of pH and saturation state up-regulation. *Geochimica et Cosmochimica Acta* **87,** 21–34 (2012).
61. Gagnon, A. C., Adkins, J. F., Erez, J. & Eiler, J. M. Sr/Ca sensitivity to aragonite saturation state in cultured subsamples from a single colony of coral: Mechanism of biomineralization during ocean acidification. *Geochemica et Cosmochimica Acta* **105,** 240–254 (2013).
62. Rae, J. W. B. in *Boron Isotopes* 107–144 (2017).
63. Wang, X. T. *et al.* Deep-sea coral evidence for lower Southern Ocean surface nitrate concentrations during the last ice age. *PNAS* **114,** 3352–3357 (2017).